

Nanoscale

Accepted Manuscript



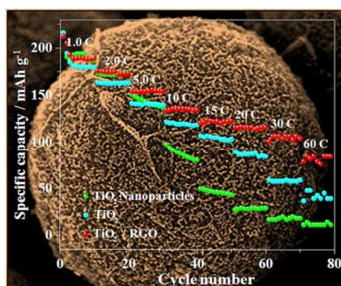
This is an *Accepted Manuscript*, which has been through the Royal Society of Chemistry peer review process and has been accepted for publication.

Accepted Manuscripts are published online shortly after acceptance, before technical editing, formatting and proof reading. Using this free service, authors can make their results available to the community, in citable form, before we publish the edited article. We will replace this *Accepted Manuscript* with the edited and formatted *Advance Article* as soon as it is available.

You can find more information about *Accepted Manuscripts* in the [Information for Authors](#).

Please note that technical editing may introduce minor changes to the text and/or graphics, which may alter content. The journal's standard [Terms & Conditions](#) and the [Ethical guidelines](#) still apply. In no event shall the Royal Society of Chemistry be held responsible for any errors or omissions in this *Accepted Manuscript* or any consequences arising from the use of any information it contains.

Table of Content



A facile method synthesis of reduced graphene oxide wrapped mesoporous TiO_2 microspheres, which show excellent electrochemical performance, at 60 C rate, a high discharge capacity of 83.6 mAh g^{-1} .

Cite this: DOI: 10.1039/c0xx00000x

www.rsc.org/xxxxxx

FULL PAPER

Synthesis and Optimizable Electrochemical Performance of Reduced Graphene Oxide Wrapped Mesoporous TiO₂ Microspheres

Xiao Yan^a, Yanjuan Li^b, Fei Du^a, Kai Zhu^a, Yongquan Zhang^a, Anyu Su^a, Gang Chen^{a,c}, and Yingjin Wei^{*a}⁵ Received (in XXX, XXX) Xth XXXXXXXXX 20XX, Accepted Xth XXXXXXXXX 20XX

DOI: 10.1039/b000000x

A facile microwave solvothermal process is developed to prepare anatase TiO₂ anode material that maintaining multiple properties including high surface area, high crystallinity, uniform mesoporous, perfect microspheres and uniform particle size. Using this fine anatase TiO₂ product, a TiO₂/RGO (RGO: reduced graphene oxide) hybrid material is prepared under UV-light irradiation. Incorporation of RGO improves the electrochemical kinetics of the TiO₂ microspheres, which results in superior electrochemical performance in terms of specific capacity, rate capability and cycle stability. The material shows a discharge capacity of 155.8 mAh g⁻¹ at the 5 C rate. Even at the 60 C rate, a high discharge capacity of 83.6 mAh g⁻¹ is still obtained which is two times higher than that of pristine mesoporous TiO₂.

1. Introduction

The production of titanium dioxide (TiO₂) has become the third-largest industry in the world for inorganic raw materials with over six million tons produced per year. The importance of TiO₂ is obvious; from its diverse range of commercial applications such as whiteners in paint or as an abrasive in common products such as toothpaste. More importantly, recent studies on solar cells, lithium ion batteries, hydrogen production and photogradation of organic pollutants have shown considerable promise of TiO₂ in energy and environmental-related fields.¹⁻⁴ For example, as an anode material for lithium ion batteries, TiO₂ shows several advantages such as long cycle life, low cost and environmental benign. Moreover, the working voltage of TiO₂ (~ 1.6 V vs. Li/Li⁺) can efficiently avoid the formation of solid electrolyte interface (SEI) layers and lithium plating on the anode, which improves the safety of the batteries as compared with the traditional graphite anode.⁵ Among all the TiO₂ polymorphs, anatase is generally considered as the most suitable one for lithium ion batteries. But, the

intrinsic low electronic conductivity of TiO₂ is an impediment to its practical applications. Recently, various solutions such as doping of foreign atoms (N, Nb, W et al.)⁶⁻⁸ and combination with high conductive materials (Au, RuO₂, CNT et al)⁹⁻¹¹ have been applied to circumvent the above drawback of anatase TiO₂. Among all the available conductive additives, graphene which has high conductivity, large surface area and excellent structural stability has attracted particular attention. In general, graphene in the electrodes can act as both conductive channels and an elastic buffer to accommodate the volume change during repeated lithium uptake and removal, even at a low weight fraction. Consequently, modification of TiO₂ with graphene has attracted broad interest in the battery community.¹²⁻¹⁴

In addition, the effectiveness of TiO₂ for battery performance varied considerably with its surface area, porosity, crystallinity and, importantly, the morphology of the material. In this regard, mesoporous TiO₂ with micron-sized spherical architecture is highly attractive. The small primary crystals of the mesoporous material provide short diffusion length for Li⁺ ions. And the mesoporous structure allows the electrolyte to wet the electrode effectively. Moreover, the micron-sized spherical particles have some additional advantages of high tap density, easy processing and good stress-strain relief during lithium insertion/extraction reactions. Thus, many efforts have been done to prepare spherical mesoporous TiO₂ materials. For example, Shao et al. prepared TiO₂ mesoporous microspheres by the co-precipitation method. The material exhibited a discharge capacity of 150 mAh g⁻¹ at the 1.2 C rate, which is not very satisfactory for high rate applications.¹⁵ Lee et al. synthesized mesoporous TiO₂ microspheres by the solvothermal method. The material showed a high discharge capacity of 125 mAh g⁻¹ at the 10 C rate.¹⁶ But, the TiO₂ particles have a non-uniform size distribution. In addition, the solvothermal treatment is time-consuming which needs more

³⁵ ^a Key Laboratory of Physics and Technology for Advanced Batteries (Ministry of Education), College of Physics, Jilin University, Changchun 130012, P. R. China.

E-mail: yjwei@jlu.edu.cn

⁴⁰ ^b College of Material Science and Engineering, Key Laboratory of Automobile Materials of Ministry of Education, Jilin University, Changchun 130012, P. R. China

^c State Key Laboratory of Superhard Materials, Jilin University, Changchun 130012, P. R. China

Electronic Supplementary Information (ESI) available: [TGA of TiO₂/RGO sample, XPS and AFM of the graphene oxide, SEM of TiO₂ nanoparticles, SEM of the TiO₂ and TiO₂/RGO after cycles, Rate performance of RGO, Rate performance of TiO₂/RGO with different contents of RGO]. See DOI: 10.1039/b000000x/

than ten hours.

Recently, microwave solvothermal method has become an efficient alternative to the traditional solvothermal method as it allows for rapid heating to the required temperature and extremely rapid rate of crystallization. Microwave solvothermal has been widely applied in the preparation of TiO₂ materials. But most of the TiO₂ products are ordinary nanoparticles.¹⁷⁻²¹ To our knowledge, a facile microwave solvothermal process has not been developed to prepare TiO₂ materials that maintaining multiple properties including high surface area, high crystalline, uniform mesoporous, perfect microspheres and uniform particle size. In this work, we synthesized mesoporous anatase TiO₂ microspheres via a sol-gel process followed by microwave solvothermal reaction. Using this fine anatase TiO₂ product, a TiO₂/RGO (RGO: reduced graphene oxide) hybrid material was prepared under UV-light irradiation. The material shows excellent electrochemical performance with high capacities, good rate performance and long cycle life which is very attractive for lithium ion batteries.

2. Experimental Section

2.1. Synthesis of mesoporous TiO₂ microspheres

First, bare amorphous TiO₂ microspheres were prepared by the sol-gel method using titanium (IV) isopropoxide (TIP) as a precursor and hexadecylamine (HDA) as a structure-directing agent.^{22, 23} Then, crystalline TiO₂ microspheres were prepared by the microwave solvothermal reaction method. Typically, 0.5 g amorphous TiO₂ microspheres were dispersed into a solution containing 20 mL ethanol and 10 mL deionized water. The mixture was transferred into a 100 mL Teflon vessel and treated by microwave irradiation at 160 °C for 90 min. Then, the precipitation powder was collected by centrifugation, washed with ethanol and dried at room temperature. The final powder was calcined at 500 °C for 2 h in air to remove the organic components.

2.2. Synthesis of Reduced Graphene Oxide wrapped mesoporous TiO₂ microspheres

The graphene oxide (GO) were produced from natural graphite flakes (Sigma-Aldrich, < 20 μm) by a modified Hummers method.^{24, 25} The TiO₂/RGO composite was prepared by the UV-assisted photocatalytic method. Typically, 0.1 g TiO₂ microspheres were dispersed into 20 mL ethanol. Then, 1 mL of 3-aminopropyl-trimethoxysilane (APTMS) was added, and refluxed at 80 °C for 4 h, followed by sufficient wash with ethanol. Afterwards, the APTMS-treated TiO₂ microspheres were added into a certain amount of GO suspension under ultrasonication. The yellow suspension was then irradiated under UV-light for 2 h with constant magnetic stirring. The as-prepared TiO₂/RGO powder was then washed with deionized water and dried at 100 °C overnight.

2.3. Material characterizations

X-ray diffraction (XRD) of the samples was measured on a Bruker AXS D8 X-ray diffractometer with Cu-Kα X-ray source operating at 40 kV and 100 mA. X-ray photoelectron spectroscopy (XPS) was performed on an ESCALAB spectrometer using Mg-Kα light source. Atomic force microscope

(AFM) images were obtained by a Bruker Dimension Icon scanning probe microscope. The thermogravimetric analysis (TGA) was performed on a SDTO600 thermoanalyzer in air flow at the heating rate of 10 °C min⁻¹. The morphologies of the materials were observed by field emission scanning electron microscope (FESEM, JEOL JSM-6700F) and transmission electron microscope (TEM, FEI Tecnai G2). Nitrogen adsorption and desorption isotherms were measured at 77 K on a Micromeritics ASAP 2010 instrument. Specific surface area calculations were made using the Brunauer-Emmett Teller (BET) method. The pore-size distribution (PSD) curves were calculated from the isotherm using the BJH (Barrett-Joyner-Halenda) algorithm. The electrical conductivities of the materials were measured by the four-point-probe method using the Lake Shore PT-103 instrument.

2.4. Electrochemical measurements

The electrochemical experiments were performed using 2032-type coin cells, with metallic lithium foil served as the counter electrode. The working electrode was prepared by mixing 80 wt.% of active material, 10 wt.% of super P conductive additive and 10 wt.% of poly-vinylidene fluoride (PVDF) which was pasted onto a copper current collector. The loading mass of active material was 1~2 mg/cm². The working electrode and counter electrode were separated by Celgard 2400 membrane. A 1 mol·L⁻¹ lithium hexafluorophosphate (LiPF₆) solution dissolved in ethylene carbonate (EC), dimethyl carbonate (DMC) and ethylmethyl carbonate (EMC) (EC: DMC: EMC = 1: 1: 8) was used as the electrolyte. The battery cells were assembled in an argon-filled glovebox. Galvanostatic charge-discharge was measured on a LAND (Wuhan, China) battery tester in the voltage window of 1.0-3.0 V versus Li/Li⁺. Cyclic voltammetry (CV) and electrochemical impedance spectroscopy (EIS) were performed on a VSP multichannel potentiostatic-galvanostatic system (Bio-Logic SAS, France). The impedance spectra were recorded by applying an *ac* voltage of 5 mV in the frequency range from 200 kHz to 10 mHz.

3. Results and discussion

3.1. Structure and morphology analysis

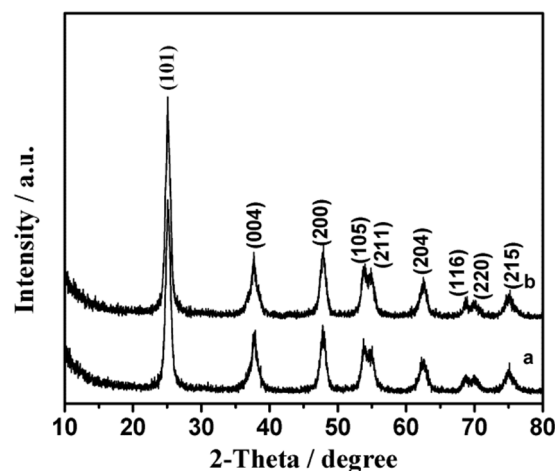


Fig. 1 XRD patterns of the (a) TiO₂ and (b) TiO₂/RGO samples.

Fig.1 shows the XRD patterns of the TiO₂ and TiO₂/RGO samples. All the identified peaks can be perfectly indexed to anatase TiO₂ with the space group of I4₁/amd (JCPDS No. 21-1272). The lattice parameters of the samples are determined by the Celref Program, which are identical for both samples, i.e. $a = 3.785 \text{ \AA}$ and $c = 9.514 \text{ \AA}$. The average crystallite size (d) of the materials is calculated using the Scherrer's formula,²⁶ $d = k\lambda/\beta\cos\theta$, where λ is the wavelength of the X-ray radiation, β is the angular line width at half of the maximum intensity in the (101) crystal facet, θ is the Bragg angle and k is a constant which is 0.9. Calculation shows that both samples have similar average crystallite size of 9.28 nm. Thus, combination with RGO does not influence the crystal structure of the host TiO₂ material. It is noticed that in the case of TiO₂/RGO, no XRD peak corresponding to the stacking of RGO layers (normally appears at $\sim 25^\circ$) is visible which may be due to the overlapping of the RGO stacking diffraction with the (101) peak of TiO₂. The RGO content in the TiO₂/RGO sample is determined by thermogravimetric analysis (TGA) (Fig. S1b, Supporting Information). Apparently, a large weight loss can be observed between 100 °C and 650 °C, indicating that the total amount of RGO in the sample is 8.9 wt%. The weight loss below 100 °C is due to the evaporation of adsorbed moisture, considering the high surface area of the sample.

To investigate the chemical nature of the TiO₂/RGO sample, XPS was performed which provides an exact elemental composition in the top 0-12 nm depth of the sample surface.²⁷ The XPS survey (Fig. 2a) confirms the C, O and Ti composition in the sample. The high resolution XPS spectra of graphene oxide (GO, Fig. S2, Supporting Information) shows typical peaks at 284.72 eV, 285.65 eV, 287.46 and 288.94 eV from graphitic C=C/C-C, C-O, C=O and COOH bonds, respectively.²⁵ After reduction, the peaks from the oxygen containing functional groups are significantly weakened which confirms the successful reduction of GO (Fig. 2b). It is worth noting that the RGO in the composite has very few residual oxygen-containing functional groups, with a C/O ratio of 7.92 after subtracting the oxygen content from the C 1s XPS spectra; therefore, a good electrical conductivity is expected.^{28, 29} The O 1s spectra shows two peaks at 532.04 eV and 530.27 eV, which arise from the RGO and the Ti-O bond, respectively (Fig. 2c). The Ti 2p XPS spectra exhibits two characteristic peaks at 464.79 eV and 459.08 eV, corresponding to the Ti 2p_{3/2} and Ti 2p_{1/2} spin-orbit peaks of TiO₂ (Fig. 2d). The morphology and microstructure of the samples are studied by FE-SEM and TEM. It is seen from FE-SEM that the pristine TiO₂ sample contains uniform and monodisperse spherical particles with diameter about 500 nm (Fig. 3a). TEM shows each

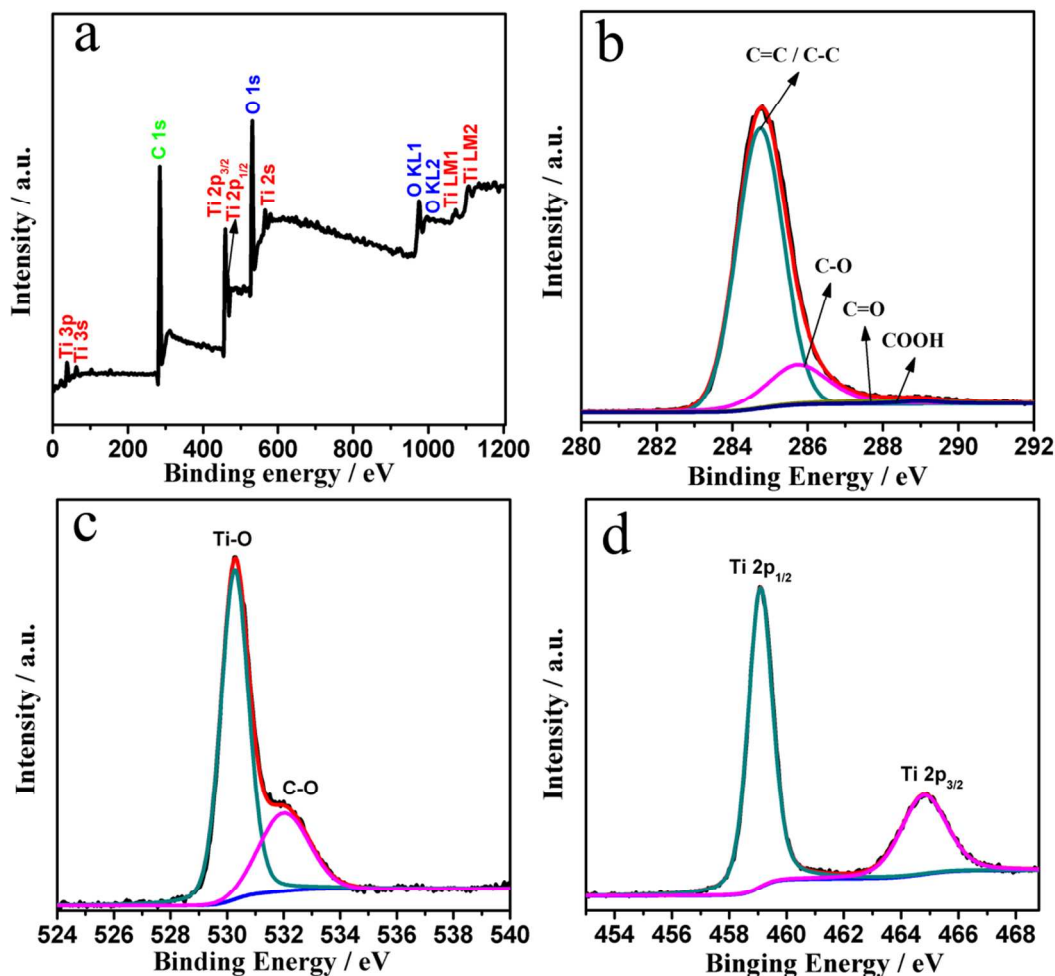


Fig. 2 XPS patterns of the TiO₂/RGO sample, (a) survey; (b) C_{1s}; (c) O_{1s}; (d) Ti_{2p}

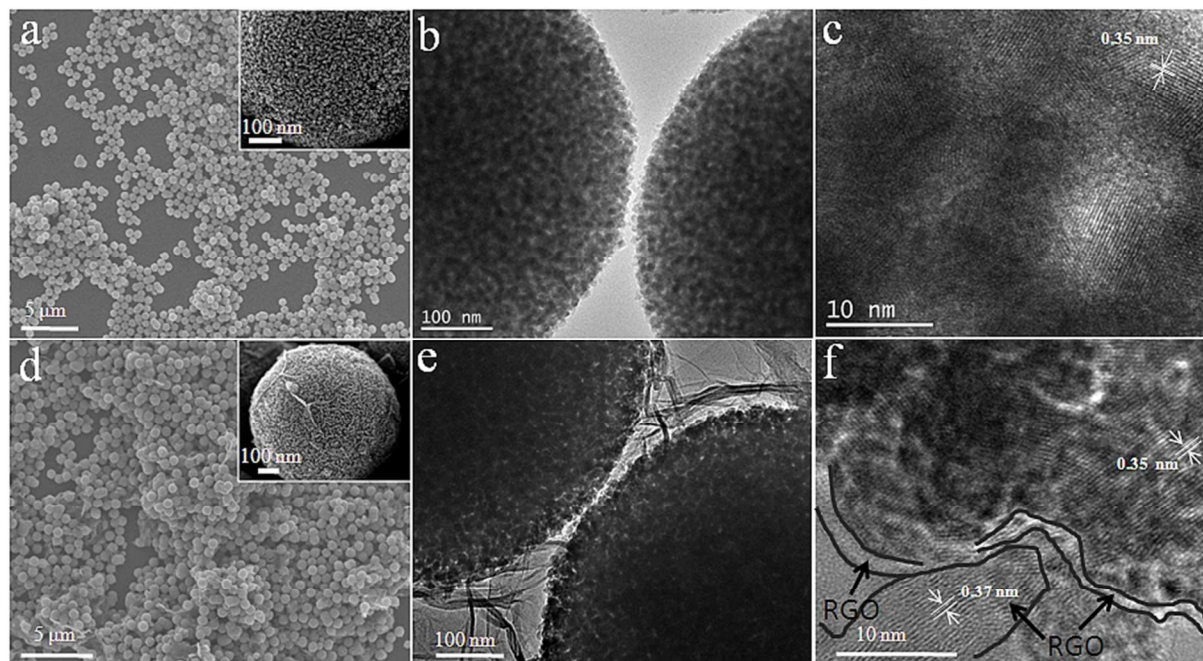


Fig. 3 FE-SEM, TEM and HRTEM images of samples (a, b, c) TiO_2 and (d, e, f) TiO_2/RGO . Insets in (a) and (d) are the corresponding high-magnification SEM images.

microsphere has a hierarchical structure that consisted of interconnected nanocrystals. Disordered mesopores are abundant throughout the microsphere (Fig. 3b). TEM and high resolution TEM reveals that the size of primary crystals is about 10 nm which is consistent with that calculated from the XRD broadening data. The clear lattice fringes of 0.35 nm corresponds well with the interplanar spacing of the anatase (101) planes.

The spherical shape of TiO_2 is maintained well when it is incorporated with RGO (Figure 3d). FE-SEM shows that the surface of the microspheres is successfully wrapped by RGO. In addition, abundant wrinkled RGO sheets fill in the space of the material that effectively link the TiO_2 microspheres (Figure 3e). For a battery electrode, this morphology can facilitate the transport of electrons thus leads to good electrochemical performance. AFM shows that the GO sheets have a 2D feature containing micro-sized flakes with thickness of ~ 1 nm, characteristic of GO mono-layers (Figure S3, Supporting Information).³⁰ From the FE-SEM and TEM images one can see that the RGO sheets are flexibly winded over the TiO_2 sphere surface. Under high resolution TEM (Figure 3f), the distance of the visible lattice fringes in the RGO sheet is measured to be 0.37 nm which is in agreement with the RGO (002) planes.^{28, 31} The RGO sheet that wrapping over the TiO_2 spheres has a thickness of ~ 2 nm while that filling in the material space has a thickness of ~ 10 nm, both of which are thicker than the GO mono-layers. This can be attributed to the stacking of RGO sheets due to the van der Waals interactions.³² In addition, the van der Waals interactions also indirectly cause the gathering of the TiO_2 spheres. As a result, the TiO_2/RGO sample seems to be denser than the pristine TiO_2 in condition that the samples are ultrasonic treated in the same way before FE-SEM and TEM analysis. The

uniform distribution of RGO in the TiO_2 microspheres is believed to enhance the electrical conductivity of the material. Measurement shows that the electrical conductivity of TiO_2 is $1.06 \times 10^{-9} \text{ s cm}^{-1}$, which fits well with that reported in the literature.³³ After the addition of RGO, the electrical conductivity is significantly increased by seven orders of magnitude, i.e. to $4.61 \times 10^{-2} \text{ s cm}^{-1}$.

The specific surface area and pore size distribution of the samples were further investigated by nitrogen adsorption-desorption isotherms as shown in Fig. 4. The samples show an IV-type isotherm curve with a H4 hysteresis loop in the range of 0.5-1.0 P/P_0 , which is indicative of mesoporosity. The pore size distribution plots are calculated from the desorption isotherm

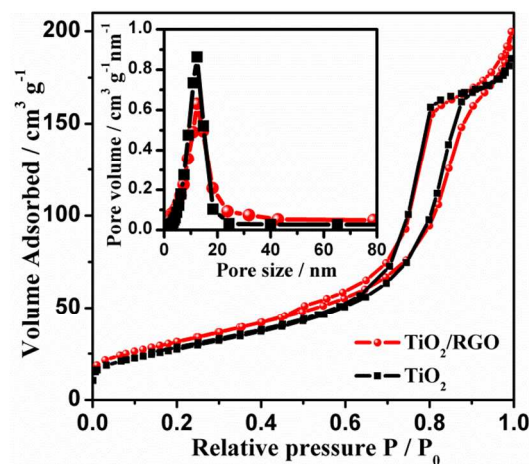


Fig. 4 Nitrogen adsorption-desorption isotherm curves of TiO_2 and TiO_2/RGO samples. Insets show their pore-size distributions.

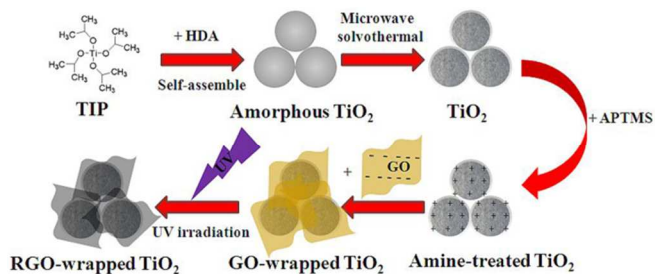


Fig. 5 Schematic illustration of the formation mechanism of TiO_2/RGO

using the Barrett-Joyner-Halenda (BJH) model (inset of Fig. 4). Both samples exhibit uniform mesopores with an average pore diameter of 12.5 nm. This indicates that RGO does not affect the mesoporous property of the TiO_2 microspheres. The standard multipoint Brunauer-Emmett-Teller (BET) method is used to calculate the specific surface area of the materials. It shows that the specific surface area of TiO_2 is $101 \text{ m}^2 \text{ g}^{-1}$. The TiO_2/RGO sample possesses a higher specific surface area of $115 \text{ m}^2 \text{ g}^{-1}$, which may be attributed to the contribution of RGO. Based on the above analysis, a formation mechanism of the TiO_2/RGO hybrid material is illustrated in Fig. 5 and described step by step as following: (Step 1) it involves the hydrolysis of titanium (IV) isopropoxide (TIP) during the sol-gel process. With the aid of hexadecylamine (HDA) which acts as a structure-directing agent, the hydrolysis product tends to self-assemble into amorphous TiO_2 microspheres;²³ (Step 2) the amorphous TiO_2 crystallizes into TiO_2 microspheres after the microwave solvothermal reactions followed by the calcination treatment; (Step 3) the surface of the TiO_2 microspheres is proton-activated in the 3-aminopropyl-trimethoxysilane (APTMS) solution; (Step 4) in the TiO_2+GO suspension, the GO sheets self-wrap over the TiO_2 microspheres as a result of the electrostatic interactions between the negative charges on GO and the positive charges on TiO_2 ; (Step 5) under UV-light irradiation, both the GO sheets on TiO_2 and those still in the suspension are reduced by the photo-excited electrons.²⁷ As the reduction proceeds, the RGO sheets are able to stack under the van der Waals interactions leading to

the thickening of the RGO sheets.

3.2. Electrochemical performance

The electrochemical properties of the TiO_2 and TiO_2/RGO samples were studied in the potential window of 1.0-3.0 V. The charge-discharge experiments were firstly performed at the 1C rate ($I = 168 \text{ mA g}^{-1}$), and then the current rate was gradually increased to 60 C ($I = 10.08 \text{ A g}^{-1}$). Fig. 6a presents the charge-discharge profiles of the materials at the 1 C, 10 C and 20 C rates. It has reported that the lithium insertion into anatase TiO_2 is mainly involved in the two-phase reaction between the TiO_2 and $\text{Li}_{0.5}\text{TiO}_2$ phases, resulting in a theoretical capacity of 168 mAh g^{-1} .³⁴ However, the 1C rate capacities of the TiO_2 and TiO_2/RGO samples are much higher than the theoretical capacity. Apparently, each discharge profile can be divided into three stages. The first stage is marked by a fast voltage decrease from the open-circuit potential to 1.7 V forming a solid solution phase. The second stage is the plateau region at $\sim 1.7 \text{ V}$, reflecting a two-phase reaction between the TiO_2 and $\text{Li}_{0.5}\text{TiO}_2$ phases.³⁵ A slope-like region is observed below 1.7 V which is due to the interfacial Li^+ ion storage similar to the capacitive behaviour of nano materials.^{15,16} This interfacial Li^+ ion storage contributes to the additional discharge capacity of the samples as observed in many other nano TiO_2 materials.³⁶⁻³⁸ It is seen that the capacity of the slope-like region for the TiO_2/RGO sample is slightly larger than that of pristine TiO_2 , which is probably due to its larger surface area. A large irreversible capacity is observed in the first cycle not only for TiO_2 (columbic efficiency 88.6%) but also for TiO_2/RGO (columbic efficiency 84.4%). This can be due to the Li^+ storage into the irreversible sites. In addition, the adsorbed moisture in the mesoporous samples will cause the decomposition of the electrolyte, which also gives rise to some irreversible capacity.³⁴ The smaller initial columbic efficiency of TiO_2/RGO may be due to the bad electrochemical performance of the RGO component as will be shown below. However, after several cycles, the columbic efficiency significantly increases to $\sim 100\%$ indicating good reversibility of the electrochemical

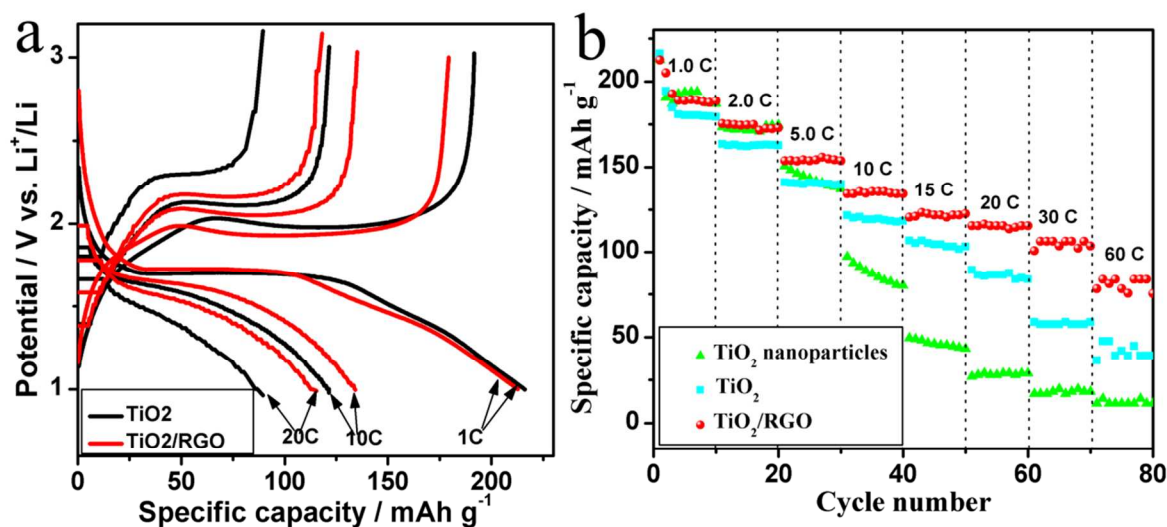


Fig. 6 (a) Charge-discharge profiles of TiO_2 and TiO_2/RGO at 1 C, 10 C and 20 C rate, and (b) Rate dependent cycling performances of TiO_2 and TiO_2/RGO , together with that of lab-prepared ordinary TiO_2 nanoparticles.

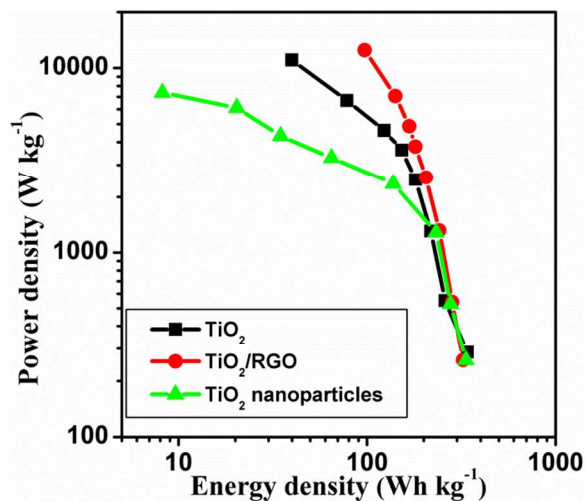


Fig. 7 Ragone plots of TiO₂ and TiO₂/RGO, together with that of lab-prepared ordinary TiO₂ nanoparticles.

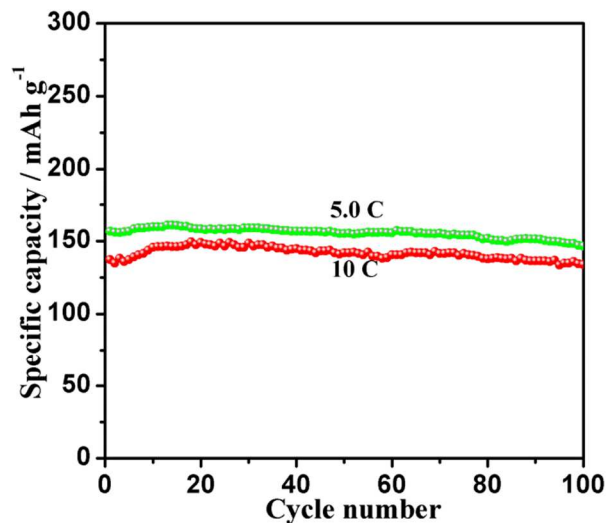


Fig. 8 Cycling performance of the TiO₂/RGO sample at the 5C and 10 C rates

reactions.

The rate dependent cycling performance of the TiO₂ and TiO₂/RGO samples is displayed in Fig. 6b, together with that of lab-prepared ordinary TiO₂ nanoparticles (with spherical shape and 20 nm in size, Fig. S4, Supporting information) for sake of comparison. The discharge capacities of the three samples are similar at low rates. When the charge-discharge rate increases to 10 C, the discharge capacities of the mesoporous TiO₂ and TiO₂/RGO samples is remarkably higher than that of the TiO₂ nanoparticles. This can be attributed to the smaller crystallite size of the mesoporous TiO₂ which provides not only shorter pathway for Li⁺ ion diffusion but also larger surface area for interfacial Li⁺ ion storage. More importantly, the hierarchical pore structure of the mesoporous samples are uniform in size and shape, as well as being connected in a continuous 3D network. This unique structure is beneficial for soaking of the electrolyte, thus facilitating the Li⁺ ion transportation through the electrolyte.

The effects of RGO in the rate capability of mesoporous TiO₂ are also significant. With the incorporation of RGO, the discharge capacity is substantially increased compared with the pristine mesoporous TiO₂, especially at higher charge-discharge rates. For example, the discharge capacity of TiO₂/RGO at the 60 C rate is 83.6 mAh g⁻¹, which is two times higher than that of mesoporous TiO₂. The specific energy density (E) and specific power density (P) are calculated from discharge profiles and displayed as Ragone plot as shown in Fig. 7. Apparently, the maximum specific energy density of 97.1 Wh kg⁻¹ and the highest specific power density of 12.5 kW kg⁻¹ are achieved using our TiO₂/RGO sample. After the charge-discharge experiment, the mesoporous TiO₂ and TiO₂/RGO electrodes are studied by SEM (Fig. S5, Supporting information). It shows that the TiO₂ microspheres in the two electrodes are almost un-destroyed, highlighting the excellent structure stability of the materials. Further, the cycling performance of the TiO₂/RGO sample at the 5 C and 10 C rates are measured and shown in Fig. 8. It is seen that the material shows good capacity retention with very small capacity loss after

45 100 cycles.

RGO is also known as a Li⁺ ion storage material. To identify the capacity contribution from RGO in the TiO₂/RGO sample, the Li⁺ insertion/extraction behavior of pure RGO is studied at different C rate (1C=168mA g⁻¹) (Fig. S6, Supporting information). An initial discharge capacity of 135.7 mAh g⁻¹ is obtained between 1.0 V and 3.0 V with a small coulombic efficiency of 75 %. As a result, TiO₂/RGO has smaller initial coulombic efficiency than that of pristine TiO₂. The discharge capacity rapidly decreases to 94.4 mAh g⁻¹ within 5 cycles. At higher charge-discharge rates, RGO has almost negligible discharge capacities. Thus, the high discharge capacity of TiO₂/RGO is not due to the capacity contribution from RGO, but can only be due to its high electronic conductivity which improves the Li⁺ ion storage in TiO₂. We also studied the charge-discharge performance of other TiO₂/RGO samples with different RGO contents (Fig. S7, Supporting information). The result verifies again that incorporation of RGO indeed improves the electrochemical performance of TiO₂. But too much of RGO (e.g. 11.2 wt.%) seems no benefit for obtaining better electrochemical performance.

Fig. 9 compares the CV curves of the TiO₂ and TiO₂/RGO samples at different scan rates in the voltage range of 1.0-3.0 V. All the CV curves are characterized by a couple of cathodic/anodic peaks, which is attributed to the Li⁺ insertion/extraction from the tetragonal TiO₂ and the orthorhombic Li_{0.5}TiO₂ phases. In addition, the small current humps at the left side of the cathodic/anodic peaks are due to the interfacial Li⁺ ion storage. When increasing the scan rate, the TiO₂/RGO electrode maintains a symmetrical CV curve; however the CV curve changes greatly for the TiO₂ electrode. We cannot even see the cathodic peak clearly when the scan rate reaches 1.0 mV s⁻¹. Well-shaped CV curves for the TiO₂/RGO electrode indicate its good electrochemical reversibility and rate capability. The cathodic or anodic peak in the CV curve has been used to evaluate the diffusion kinetics of Li⁺ insertion materials. The

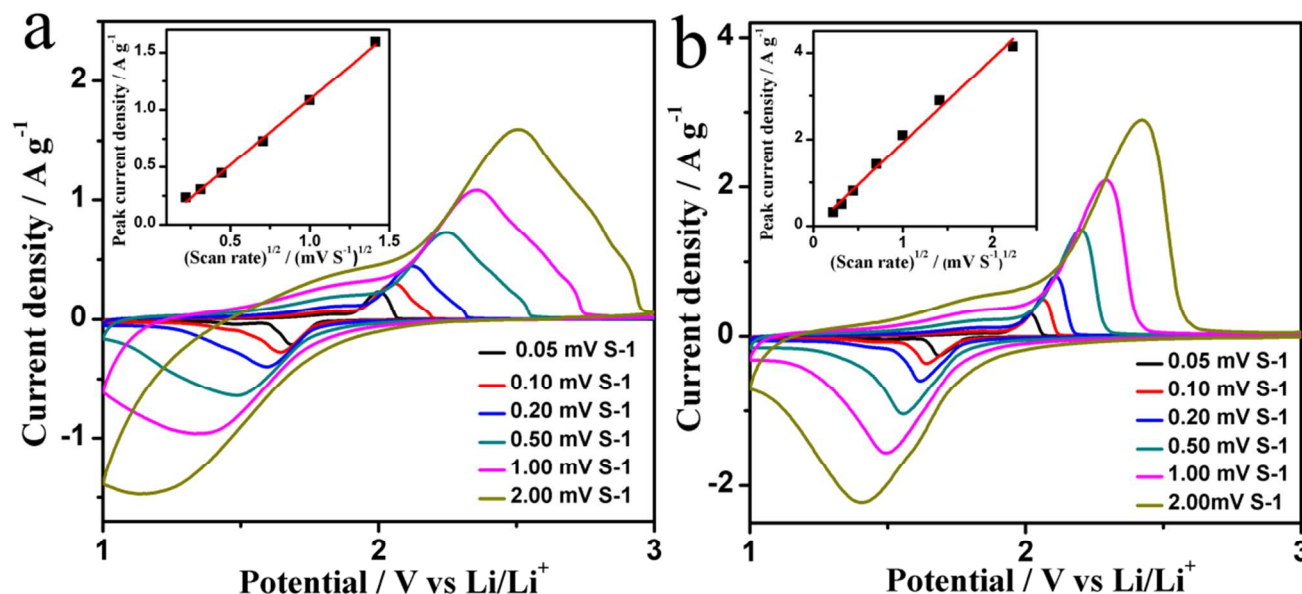


Fig. 9 CV curves of the TiO₂ and TiO₂/RGO samples at different scan rates. Inset displays the linear fitting of peak current density versus square root of the scan rate.

peak current I_p can be expressed by the equation (1),³⁹
 $I_p = 2.69 \times 10^5 n^{3/2} S D_{Li}^{1/2} v^{1/2} C$ (1)
 where n is the number of electrons per species reaction, S is the active surface area of the electrode, D_{Li} is the Li⁺ diffusion coefficient, C is the concentration of Li⁺ ions in the electrode, and v is the scan rate. We assume that the TiO₂ and TiO₂/RGO electrodes have the same active surface area (S) because the two materials have similar specific area and the electrodes are prepared in the same way. In addition, at the low scan rate of 0.05 mV s⁻¹ to 2.0 mV s⁻¹ (approximately corresponding to the 0.1C to 4C rates), the two electrodes have similar Li⁺ ion capacities as shown in Fig. 6. From the inset of Fig. 8, the peak current density shows a linear relationship versus square root of the scan

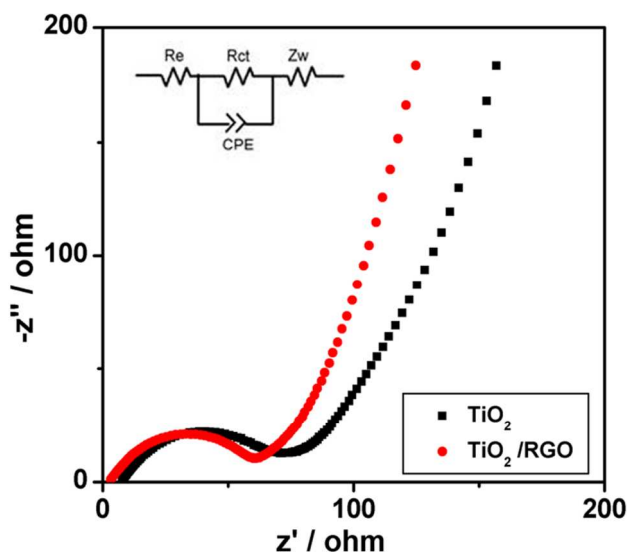


Fig. 10 Nyquist plots of the TiO₂ and TiO₂/RGO samples. Inset shows the equivalent circuit.

rate. Therefore, we can easily compare the Li⁺ diffusion coefficient of TiO₂ and TiO₂/RGO using the above equation. It shows that the Li⁺ diffusion coefficient of TiO₂/RGO is 3.7 times higher than that of pristine TiO₂. The Li⁺ diffusion coefficient can be expressed as a product of a self-diffusion coefficient $D_{Li(\text{self})}$ and a Wagner factor Φ , equation (2).⁴⁰
 $D_{Li} = D_{Li(\text{self})} \cdot \Phi$ (2)
 $D_{Li(\text{self})}$ is related to the ionic mobility or viscosity of an active material, which is majorly determined by the structural properties of the material. The Wagner factor Φ fundamentally depends on the mobilities and concentrations of Li⁺ ions and electrons in the active material. It generally reflects the influence of electron motion on the diffusion of Li⁺ ions by the effect of internal electrical field.^{41,41} Since the crystal structure and microstructure of the TiO₂ microspheres are not changed by the addition of RGO, the self-diffusion coefficient of TiO₂/RGO should be very similar with that of pristine TiO₂. Therefore, the larger Li⁺ diffusion coefficient of TiO₂/RGO should be mainly related with the highly conductive RGO which accelerates the diffusion of Li⁺ ions through a stronger internal electrical field.

In order to gain insight into the remarkable rate performance of TiO₂/RGO, we carried out AC impedance measurements at the state of charge of 3.0 V after the first cycle. As shown in Fig. 10, the Nyquist plots show that the diameter of the semicircle for TiO₂/RGO in the high-to-medium frequency region is much smaller than that of pristine TiO₂, which suggests that TiO₂/RGO possesses lower ohmic resistance (R_e) and charge transfer resistance (R_{ct}). The exact kinetic differences between the TiO₂/RGO and TiO₂ microspheres are inspected by modeling the Nyquist plots based on the equivalent circuit in the inset of Fig. 9. The values of the ohmic resistance and charge transfer resistance are 3 Ω and 60 Ω for TiO₂/RGO, which are significantly lower

than those of pristine TiO₂ (8 Ω and 84 Ω). This result validates that the RGO in TiO₂ microspheres not only improve the ohmic conductivity of the overall electrode, but also largely enhance the electrochemical activity of the TiO₂ active material.

4. Conclusion

In summary, we have successfully synthesized anatase TiO₂ and TiO₂/RGO microspheres via a sol-gel process followed by microwave solvothermal reaction. The nano sized TiO₂ crystallites provide not only short pathways for Li⁺ ion diffusion but also large surface area for interfacial Li⁺ ion storage. And their mesoporous microstructure is beneficial for soaking of the electrolyte, thus facilitating the Li⁺ ion transportation through the electrolyte. Incorporation of RGO further improves the electrochemical kinetics of the TiO₂ microspheres, which results in superior electrochemical performance in terms of specific capacity, rate capability and cycle stability. This work demonstrates the potential applications of TiO₂/RGO microspheres in high power lithium ion batteries.

Acknowledgements

This work was supported by the National Natural Science Foundation of China (No. 51272088), the National Found for Fostering Talents of Basic Science (No. J1103202), and the Research Fund for the Doctoral Program of Higher Education of China (No. 20110061130006).

References

- U. Bach, D. Lupo, P. Comte, J. E. Moser, F. Weissortel, J. Salbeck, H. Spreitzer and M. Gratzel, *Nature*, 1998, 395, 583-585.
- T. Xia, W. Zhang, J. B. Murowchick, G. Liu and X. Chen, *Adv. Energy Mater.*, 2013, 3, 1516-1523.
- K. Zhang, Q. Liu, H. Wang, R. Zhang, C. Wu and J. R. Gong, *Small*, 2013, 9, 2452-2459.
- Y. Zhang, Y. Tang, S. Yin, Z. Zeng, H. Zhang, C. M. Li, Z. Dong, Z. Chen and X. Chen, *Nanoscale*, 2011, 3, 4074-4077.
- X. Yan, Y. Zhang, K. Zhu, Y. Gao, D. Zhang, G. Chen, C. Wang and Y. Wei, *J. Power Sources*, 2014, 246, 95-102.
- Y. D. Wang, B. M. Smarsly and I. Djerdj, *Chem. Mater.*, 2010, 22, 6624-6631.
- Y. D. Wang, T. Chen and Q. Y. Mu, *J. Mater. Chem.*, 2011, 21, 6006-6013.
- W. Jiao, N. Li, L. Wang, L. Wen, F. Li, G. Liu and H. M. Cheng, *Chem. Commun.*, 2013, 49, 3461-3463.
- Y. Guo, Y. Hu, W. Sigle and J. Maier, *Adv. Mater.*, 2007, 19, 2087-2091.
- S. H. Nam, H. S. Shim, Y. S. Kim, M. A. Dar, J. G. Kim and W. B. Kim, *ACS Appl. Mater. Inter.*, 2010, 2, 2046-2052.
- S. Ding, J. S. Chen and X. W. Lou, *Adv. Funct. Mater.*, 2011, 21, 4120-4125.
- D. Wang, D. Choi, J. Li, Z. Yang, Z. Nie, R. Kou, D. Hu, C. Wang, L. V. Saraf, J. Zhang, I. A. Aksay and J. Liu, *ACS Nano*, 2009, 3, 907-914.
- N. Li, G. Liu, C. Zhen, F. Li, L. I. Zhang and H. M. Cheng, *Adv. Funct. Mater.*, 2011, 21, 1717-1722.
- S. Yang, X. Feng and K. Muellen, *Adv. Mater.*, 2011, 23, 3575-3579.
- J. Wang, Y. Zhou, Y. Hu, R. O'Hayre and Z. Shao, *J. Phys. Chem. C*, 2011, 115, 2529-2536.
- Y. Ma, G. Ji, B. Ding and J. Y. Lee, *J. Mater. Chem.*, 2012, 22, 24380-24385.
- S. Komarneni, R. K. Rajha and H. Katsuki, *Mater. Chem. Phys.*, 1999, 61, 50-54.
- G. J. Wilson, G. D. Will, R. L. Frost and S. A. Montgomery, *J. Mater. Chem.*, 2002, 12, 1787-1791.
- A. V. Murugan, V. Samuel and V. Ravi, *Mater. Lett.*, 2006, 60, 479-480.
- G. J. Wilson, A. S. Matijasevich, D. R. G. Mitchell, J. C. Schulz and G. D. Will, *Langmuir*, 2006, 22, 2016-2027.
- K. Ding, Z. Miao, Z. Liu, Z. Zhang, B. Han, G. An, S. Miao and Y. Xie, *J. Am. Chem. Soc.*, 2007, 129, 6362-6363.
- D. Chen, F. Huang, Y.-B. Cheng and R. A. Caruso, *Adv. Mater.*, 2009, 21, 2206-2210.
- D. Chen, L. Cao, F. Huang, P. Imperia, Y.-B. Cheng and R. A. Caruso, *J. Am. Chem. Soc.*, 2010, 132, 4438-4444.
- Y. Xu, H. Bai, G. Lu, C. Li and G. Shi, *J. Am. Chem. Soc.*, 2008, 130, 5856-5857.
- L. Yang, J. Kong, W. A. Yee, W. Liu, S. L. Phua, C. L. Toh, S. Huang and X. Lu, *Nanoscale*, 2012, 4, 4968-4971.
- Y. Xie and C. Yuan, *Appl. Catal. B-Environ.*, 2003, 46, 251-259.
- Y. Dai, Y. Jing, J. Zeng, Q. Qi, C. Wang, D. Goldfeld, C. Xu, Y. Zheng and Y. Sun, *J. Mater. Chem.*, 2011, 21, 18174-18179.
- Z. Wu, W. Ren, L. Gao, B. Liu, C. Jiang and H. Cheng, *Carbon*, 2009, 47, 493-499.
- Z. Wu, W. Ren, D. Wang, F. Li, B. Liu and H. Cheng, *ACS Nano*, 2010, 4, 5835-5842.
- J. Zhang, H. Yang, G. Shen, P. Cheng, J. Zhang and S. Guo, *Chem. Commun.*, 2010, 46, 1112-1114.
- H. C. Schniepp, J. L. Li, M. J. McAllister, H. Sai, M. Herrera Alonso, D. H. Adamson, R. K. Prud'homme, R. Car, D. A. Saville and I. A. Aksay, *J. Phys. Chem. B*, 2006, 110, 8535-8539.
- H. M. Liu and W. S. Yang, *Energy Environ. Sci.*, 2011, 4, 4000-4008.
- P. Ciambelli, L. Lisi, G. Russo and J. C. Volta, *Appl. Catal. B-Environ.*, 1995, 7, 1-18.
- J. Y. Shin, D. Samuelis and J. Maier, *Adv. Funct. Mater.*, 2011, 21, 3464-3472.
- Y. Li, X. Yan, W. Yan, X. Lai, N. Li, Y. Chi, Y. Wei and X. Li, *Chem. Eng. J.*, 2013, 232, 356-363.
- S. W. Kim, T. H. Han, J. Kim, H. Gwon, H. S. Moon, S. W. Kang, S. O. Kim and K. Kang, *ACS Nano*, 2009, 3, 1085-1090.
- K. Saravanan, K. Ananthanarayanan and P. Balaya, *Energy Environ. Sci.*, 2010, 3, 939-948.
- N. Li, G. M. Zhou, R. P. Fang, F. Li and H. M. Cheng, *Nanoscale*, 2013, 5, 7780-7784.
- T. Jiang, W. Pan, J. Wang, X. Bie, F. Du, Y. Wei, C. Wang and G. Chen, *Electrochim. Acta.*, 2010, 55, 3864-3869.
- C. Wagner, *J. Chem. Phys.*, 1953, 21, 1819-1827.
- P. G. Bruce, *Solid State Electrochemistry Cambridge University Press*, 1995, PP. 207.